iScience

CellPress
OPEN ACCESS

Article

HYSCORE and DFT Studies of Proton-Coupled Electron Transfer in a Bioinspired Artificial Photosynthetic Reaction Center

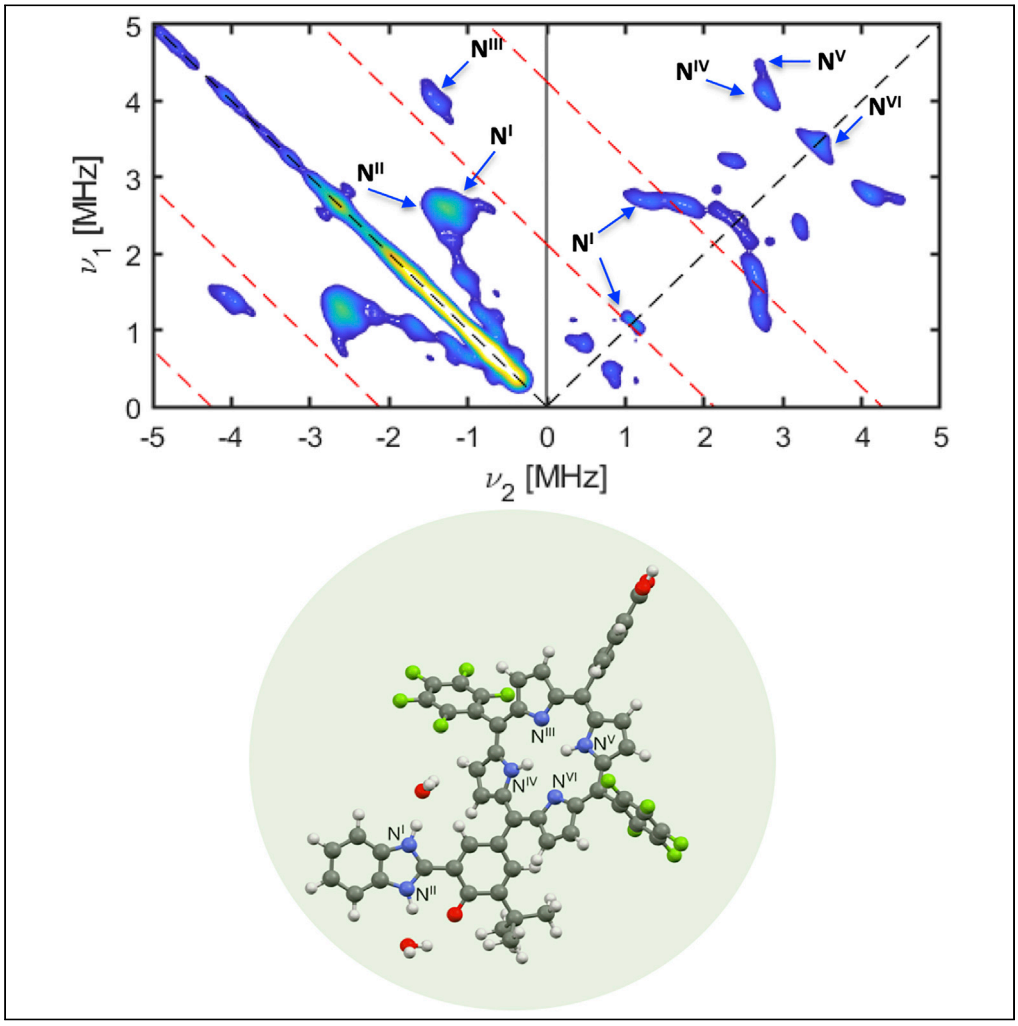

Dalvin D. Méndez-Hernández, Amgalanbaatar Baldansuren, Vidmantas Kalendra, ..., Thomas A. Moore, K.V. Lakshmi, Ana L. Moore

dalvin.mendez@upr.edu (D.D.M.-H.)
k.lakshmi04@gmail.com (K.V.L.)
amoore@asu.edu (A.L.M.)

HIGHLIGHTS

Structural factors are critical in the design of artificial photosynthetic systems

Correlation between hyperfine couplings of the N atoms and electron spin density

Spin density distribution affected by charge delocalization and explicit waters

Spin density modulation by electronic coupling as observed with P_{680} and Y_Z in PSII

Méndez-Hernández et al., iScience *23*, 101366
August 21, 2020
https://doi.org/10.1016/j.isci.2020.101366

iScience

CellPress
OPEN ACCESS

Article

HYSCORE and DFT Studies of Proton-Coupled Electron Transfer in a Bioinspired Artificial Photosynthetic Reaction Center

Dalvin D. Méndez-Hernández,[1,4,*] Amgalanbaatar Baldansuren,[2] Vidmantas Kalendra,[2] Philip Charles,[2] Brian Mark,[2] William Marshall,[2] Brian Molnar,[2] Thomas A. Moore,[3] K.V. Lakshmi,[2,*] and Ana L. Moore[3,*]

SUMMARY

The photosynthetic water-oxidation reaction is catalyzed by the oxygen-evolving complex in photosystem II (PSII) that comprises the Mn_4CaO_5 cluster, with participation of the redox-active tyrosine residue (Y_Z) and a hydrogen-bonded network of amino acids and water molecules. It has been proposed that the strong hydrogen bond between Y_Z and D1-His190 likely renders Y_Z kinetically and thermodynamically competent leading to highly efficient water oxidation. However, a detailed understanding of the proton-coupled electron transfer (PCET) at Y_Z remains elusive owing to the transient nature of its intermediate states involving $Y_Z^{\bullet}$. Herein, we employ a combination of high-resolution two-dimensional ^{14}N hyperfine sublevel correlation spectroscopy and density functional theory methods to investigate a bioinspired artificial photosynthetic reaction center that mimics the PCET process involving the Y_Z residue of PSII. Our results underscore the importance of proximal water molecules and charge delocalization on the electronic structure of the artificial reaction center.

INTRODUCTION

The photosynthetic protein complex, photosystem II (PSII), catalyzes one of the most energetically demanding reactions in nature by using light energy to drive a catalyst capable of oxidizing water (Saito et al., 2011; Shen, 2015; Suga et al., 2015; Umena et al., 2011; Young et al., 2016). Proton-coupled electron transfer (PCET) reactions, which are exquisitely tuned by smart protein matrix effects, are central to the water oxidation chemistry of PSII. Moreover, PCET is encountered in a wide variety of biological and synthetic catalysts where it diminishes the overall energetic penalty for multi-electron transfer and modulates the electrochemical driving force of reactions (Cukier and Nocera, 1998; Odella et al., 2019, 2018). In PSII, light-driven water oxidation is catalyzed in the oxygen-evolving complex (OEC) that comprises a tetranuclear manganese-calcium-oxo (Mn_4Ca-oxo) cluster with an extensive network of hydrogen (H)-bonded amino acid residues and structured water molecules (Shen, 2015). In particular, there are two symmetrically placed tyrosine residues, Y_D and Y_Z, one on each subunit of the heterodimeric core polypeptide, D2 and D1, respectively (Figure 1A) (Suga et al., 2015; Umena et al., 2011; Young et al., 2016). The function of these tyrosines is distinct as the "smart" matrix effects from the surrounding protein environment greatly influence their behavior (Barry et al., 1990; Chai et al., 2019; Debus, 1992; Styring et al., 2012). The Y_D redox is suggested to poise the catalytic Mn_4Ca-oxo cluster (Styring and Rutherford, 1987) and may be involved in the electrostatic tuning of the adjacent monomeric redox-active chlorophyll and β-carotene in a secondary photoprotection pathway (Diner and Rappaport, 2002; Rutherford et al., 2004; Saito et al., 2016). In contrast, Y_Z is kinetically competent and directly participates in water oxidation (Hoganson and Babcock, 1997; McEvoy and Brudvig, 2006, 2004). Previous biochemical, spectroscopic, and computational studies have demonstrated that both Y_D and Y_Z undergo photo-induced PCET with the formation of a neutral tyrosyl radical, $Y^{\bullet}$, but the formation and decay of the $Y_Z^{\bullet}$ is a thousand times more rapid than $Y_D^{\bullet}$ (Bertho-mieu and Hienerwadel, 2005; Chrysina et al., 2019; Faller et al., 2002; Hart and O'Malley, 2010; Hoganson and Tommos, 2004; Ishikita and Knapp, 2006; Jenson et al., 2007; Kawashima et al., 2018; Keßen et al., 2010; Sakamoto et al., 2017; Styring et al., 2012; Szczepaniak et al., 2008).

The difference in the kinetics of light-driven PCET at Y_Z and Y_D has been suggested to arise from differences in their respective microenvironment. The protein matrix surrounding Y_Z is highly hydrophilic with

[1]Department of Chemistry, University of Puerto Rico at Cayey, Cayey 00736, Puerto Rico

[2]Department of Chemistry and Chemical Biology and The Baruch '60 Center for Biochemical Solar Energy Research, Rensselaer Polytechnic Institute, Troy, NY 12180, USA

[3]School of Molecular Sciences, Arizona State University, Tempe, AZ 85287, USA

[4]Lead Contact

*Correspondence: dalvin.mendez@upr.edu (D.D.M.-H.), k.lakshmi04@gmail.com (K.V.L.), amoore@asu.edu (A.L.M.)

https://doi.org/10.1016/j.isci.2020.101366

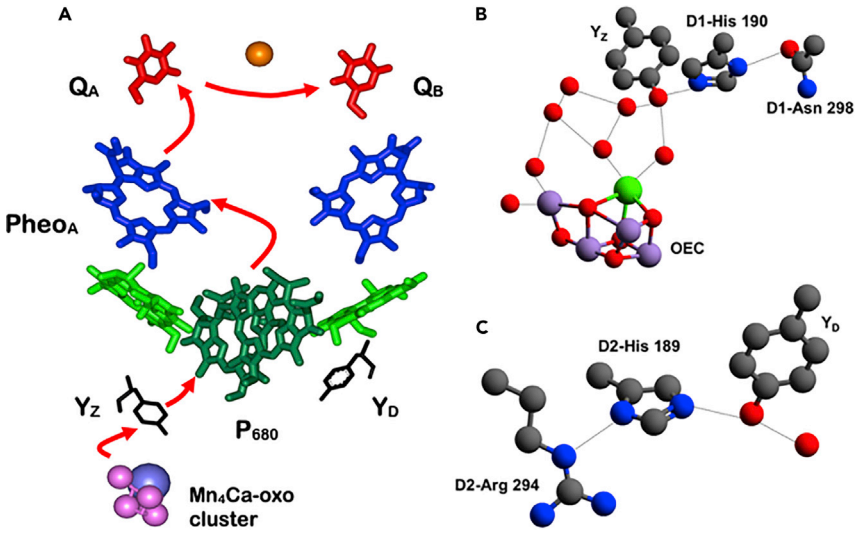

Figure 1. X-ray Crystal Structure of PSII

(A) The location of the charge-transfer cofactors that participate in the water-oxidation reaction of PSII. In the primary electron transfer (ET) pathway of PSII, the photooxidation of the primary donor, P_{680} (green), leads to the formation of the initial charge-separated state, P_{680}^{+}-$Pheo_A^{-}$ ($Pheo_A$ is shown in blue), that is rapidly stabilized by forward ET to the primary and secondary quinone acceptors, Q_A and Q_B (red), respectively. P_{680}^{+} is a strong oxidant that leads to rapid PCET at the redox-active tyrosine residue, tyrosine-Z (Y_Z) (black), which results in the oxidation of water at the Mn_4Ca-oxo cluster in the oxygen-evolving complex (OEC). The smart protein matrix in the vicinity of the redox-active (B) Y_Z and (C) tyrosine-D (Y_D) residue (black) as observed in the 1.9 Å resolution X-ray crystal structure of PSII (Umena et al., 2011).

several H-bonded water molecules, whereas the Y_D site contains a single water molecule in the X-ray crystal structure of PSII (Figures 1B and 1C) (Umena et al., 2011). Both Y_D and Y_Z are proximal to a histidine residue, D2-His189 and D1-His190, respectively, which suggests that the imidazole side chain could act as a conjugate base that accepts the proton during PCET. This is supported by recent computational studies that predict a remarkably short H-bond between Y_Z and D1-His190, which is in agreement with the X-ray crystal structure of PSII (Saito et al., 2011; Umena et al., 2011). Additionally, quantum mechanical (all-QM) and hybrid quantum mechanical/molecular modeling (QM/MM) studies have suggested that the protonation state of the conjugate base, microsolvation, and hydrogen bonding could influence the redox activity of Y_D and Y_Z (Ahlbrink et al., 1998; Chai et al., 2019; Saito et al., 2011; Sirohiwal et al., 2019). Since the $Y_Z^{\bullet}$ radical intermediate is short lived, previous mechanistic proposals for PCET were based on the dark-stable $Y_D^{\bullet}$ radical that displays slower decay kinetics. But the striking difference in the respective environments suggests that there may be important mechanistic differences in PCET at Y_Z and Y_D. It is important to understand the mechanism of PCET at Y_Z, and its role in water oxidation as the OEC of PSII is a blueprint for the design of bio-inspired molecular assemblies for new and efficient catalysts for solar fuels production that incorporate multi-electron and PCET reactions (Barber, 2008; Gust et al., 2009; Hadt et al., 2016; Megiatto et al., 2014; Maayan et al., 2018; Odella et al., 2018; Osterloh, 2008; Romero et al., 2017; Sokol et al., 2018; Zhang et al., 2015).

Since the transient $Y_Z^{\bullet}$ radical in intact PSII is not amenable to structural studies, artificial photosynthetic models of Y_Z that allow for the generation of long-lived PCET intermediates could facilitate in-depth analyses of its electronic structure. In particular, there is a need for models that mimic the key structural features of Y_Z, namely, (1) the unusually short hydrogen bond with its conjugate base partner, D1-His190 (Saito et al., 2011; Umena et al., 2011) and (2) the presence of water molecules that interact closely with both the H-bond donor and acceptor. In the present study, we demonstrate the use of an artificial photosynthetic reaction center, benzimidazole-phenol porphyrin, BiP–PF_{10}, as a model for PCET between the oxidized primary donor ($P_{680}^{\bullet+}$) and the Y_Z-D1-His190 pair in PSII (Figure 2). The BiP–PF_{10} dyad comprises a benzimidazole-phenol (BiP) moiety that is covalently attached to a high oxidation potential porphyrin (PF_{10}). Prior to PCET, the phenolic proton participates in a strong H-bond with the imino nitrogen of benzimidazole that makes the phenol essentially coplanar with the benzimidazole and mimics the Y_Z-D1-His190 interaction in PSII (Odella et al., 2018). Upon photooxidation of PF_{10}, BiP undergoes PCET that results in the formation of a long-lived radical at 77 K.

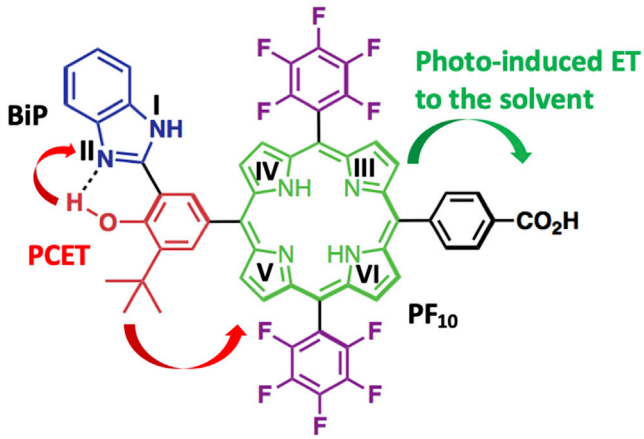

Figure 2. Schematic of the Artificial Photosynthetic Reaction Center, Benzimidazole Phenol-Porphyrin, BiP–PF_{10}

The electron withdrawing ability of the two pentafluorophenyl substituents (purple) make the porphyrin ring (green) a high oxidation potential molecule. Photooxidation of PF_{10} (depicted as a green arrow) leads to PCET at the BiP moiety (depicted as red arrows), where the electron is transferred to PF_{10}^{+} and the phenolic proton (red) is transferred to the benzimidazole imino nitrogen atom (blue). Also shown is the labeling scheme for the respective nitrogen atoms of BiP–PF_{10}.

We have previously shown that BiP acts as an effective mediator in the electrochemical oxidation of water (Zhao et al., 2012). More recently, we found that a hybrid organic/inorganic heterogeneous triad consisting of a dyad of BiP–PF_{10} linked to TiO_2 nanoparticles could undergo concerted PCET in the BiP moiety (Megiatto et al., 2014). In this system, the excitation of PF_{10} led to formation of the charge-separated state, $TiO_2^{\bullet-}$–PF_{10}–$BiP^{\bullet+}$. This study had suggested that computational models of the $(PF_{10}–BiP)^{\bullet+}$ radical in the charge-separated state, $TiO_2^{\bullet-}$–PF_{10}–$BiP^{\bullet+}$, required the inclusion of explicit water molecules in the vicinity of the phenolic proton to better describe the **g**-tensor that was obtained from high-frequency D-band (130 GHz) EPR spectroscopy.

This observation presented the possibility that solvent molecules could play an important role in the spectroscopic signatures of molecular systems and more importantly, they could influence the mechanism of PCET in BiP–PF_{10}. Similar observations have previously been reported on the role of water molecules in the prediction of the physical behavior of PSII (Barry et al., 2017; Saito et al., 2011; Sakashita et al., 2017). Recent QM/MM studies by Saito and coworkers have suggested that the structured water molecules that were observed in the 1.9 Å resolution X-ray crystal structure of PSII could play a key role in shortening the distance between Y_Z and its conjugate base partner, D1-His190. This could result in an ionic hydrogen bond (Meot-Ner, 2005), where the proton is delocalized in a nearly barrier-less potential well and the energy levels of the states with the proton associated with Y_Z or D1-His190 are essentially the same (Saito et al., 2013). This is important as the presence of a low-barrier hydrogen bond in the Y_Z-D1-His190 couple could explain the rapid kinetics of PCET as well as the lack of a pronounced deuterium isotope effect at Y_Z in comparison with that of the Y_D residue (Christen et al., 1999; Huynh et al., 2017; Jenson et al., 2007; Odella et al., 2018; Tommos et al., 1998). Additionally, the g_X component of the **g**-tensors that were determined in our previous study (Megiatto et al., 2014) for the BiP–$PF_{10}^{\bullet+}$ were lower than the corresponding values in the literature that have been attributed solely to H-bonding effects in phenoxyl groups (Saito et al., 2011). This observation suggested the presence of spin delocalization on both, the phenoxyl and porphyrin moieties, in the charge-separated state and has raised the possibility that charge delocalization could also influence the PCET reactions and thereby render the BiP an effective mediator for water oxidation.

In the present study, in order to directly probe the role of H-bonded water molecules and charge delocalization in the tuning of PCET in the artificial reaction center, BiP–PF_{10} (Figure 2), we use a combination of high-resolution two-dimensional (2D) ^{14}N hyperfine sublevel correlation (2D HYSCORE) spectroscopy and density functional theory (DFT) to determine the electronic structure of BiP–$PF_{10}^{\bullet+}$ radical that is generated following PCET by the BiP moiety. Our results indicate that it is important to include hydrogen bonding effects from explicit water molecules in order to reproduce the hyperfine coupling constants and

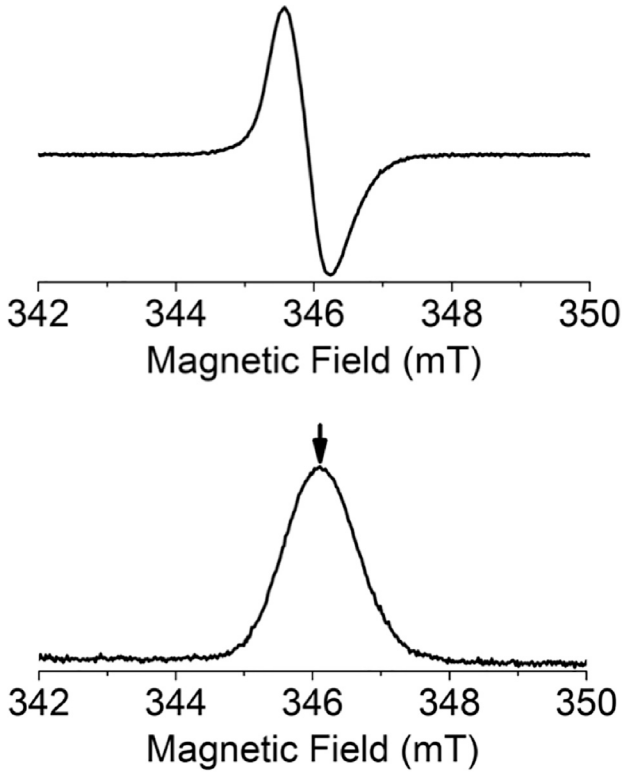

Figure 3. EPR Spectra of the PCET Radical Intermediate of Benzimidazole Phenol Porphyrin, BiP-PF_{10}

The (A) continuous-wave (*cw*) and (B) electron-spin-echo magnetic-field-sweep EPR spectrum of BiP–PF_{10}•+. The arrow in part B indicates the magnetic field position of 346.1 mT that was used for the acquisition of the 2D ^{14}N HYSCORE spectrum that is shown in Figure 4A.

delocalization of electron spin density that is observed in the experimental measurements. This study provides insight on the significance of solvation and hydrogen bonding in tuning the PCET reactions that mediate water oxidation in artificial and natural photosynthetic reaction centers.

RESULTS AND DISCUSSION

We generated the radical intermediate state of the BiP–PF_{10} dyad by illumination with white light at 77 K using DMSO as a solvent. In this case, initial light absorption leads to photoexcitation of the porphyrin, PF_{10}, which results in the formation of the photooxidized species, $PF_{10}^{\bullet+}$, through electron transfer to the solvent matrix (Charles et al., 2020; Gasyna et al., 1984; Harbour and Tollin, 1974; Linschitz and Rennert, 1952; Livingston and Ryan, 1953). This is followed by rapid PCET at the BiP moiety, which reduces the $PF_{10}^{\bullet+}$ cation to regenerate the neutral porphyrin with the formation of a phenoxyl radical where the phenolic proton is transferred to the proximal nitrogen atom on the benzimidazole (Chatterjee et al., 2013; Faller et al., 2002; Megiatto et al., 2014; Zhao et al., 2012). The presence of the continuous-wave (*cw*) and magnetic field sweep electron-spin-echo electron paramagnetic resonance (EPR) signal at a g value of 2.004 corresponding to a magnetic field position of 346.1 mT at X-band microwave frequency (9.64 GHz) confirm the formation of the BiP–$PF_{10}^{\bullet+}$ radical (electron spin, S = $^1/_2$) upon cryogenic illumination (Figures 3A and 3B). Since the structure of BiP–PF_{10} (Figure 2) exhibits partial conjugation, the g = 2.004 signal that is observed in Figures 3A and 3B could arise from overlapping spectral contributions from the distribution of the unpaired electron spin, S, of $^1/_2$ on both BiP and PF_{10} in the BiP–$PF_{10}^{\bullet+}$ radical as the respective signals are not resolved at X-band EPR frequency.

The electronic and local structure of the BiP–$PF_{10}^{\bullet+}$ radical can be determined by measuring the electron-nuclear hyperfine interactions of the unpaired electron spin (S = $^1/_2$) on the radical cation with the magnetically interacting nitrogen-14 (^{14}N) atoms (nuclear spin, I = 1). The isotropic (A_{iso}) and anisotropic components of the ^{14}N hyperfine interaction provide a measure of the distribution of the unpaired electron

spin density at the nitrogen nuclei. Additionally, the quadrupolar coupling (K) and asymmetry parameter (η) of the ^{14}N atoms reflect the interaction of the electric quadrupole moment with the electric field gradient due to the uneven distribution of electric charges around the nuclear spin. In principle, the values of K and η characterize the chemical nature of the nitrogen atom and its electronic state. Hence, these are valuable probes of the chemical nature and electric field gradient of the magnetically coupled ^{14}N atoms of BiP–$PF_{10}^{\bullet+}$. However, the weak hyperfine interactions with the ^{14}N atoms are not discernable from the line shape of the BiP–$PF_{10}^{\bullet+}$ spectra (Figures 3A and 3B) as these are completely masked by inhomogeneous broadening of the EPR signals.

In the present study, we use two-dimensional (2D) hyperfine sublevel correlation (HYSCORE) spectroscopy (see Transparent Methods) to obtain a quantitative measure of the hyperfine and quadrupolar parameters of the BiP–$PF_{10}^{\bullet+}$ radical (Chatterjee et al., 2013, 2012; Coates et al., 2015; Dikanov et al., 2019, 2000; Dikanov and Taguchi, 2018; Höfer et al., 1986; Milikisiyants et al., 2011, 2010). 2D HYSCORE spectroscopy is similar to the pulsed EPR spectroscopy methods, electron nuclear double resonance (ENDOR), and electron spin echo envelope modulation (ESEEM) (Britt, 2003; Deligiannakis et al., 2000; Harmer et al., 2009; Lakshmi and Brudvig, 2001; Prisner et al., 2001), that are used for the study of electron-nuclear hyperfine interactions in paramagnetic systems. However, in comparison with the other methods the observation of HYSCORE signals in two-dimensional (2D) frequency space results in enhanced resolution, which alleviates the problem of spectral overcrowding from the simultaneous detection of multiple nuclear spins (Harmer et al., 2009), such as the nitrogen atoms of the BiP–$PF_{10}^{\bullet+}$ radical. Additionally, the nuclear transitions are correlated in the two dimensions, which greatly facilitates the analysis and interpretation of the spectra.

The experimental 2D ^{14}N HYSCORE spectrum of the BiP–$PF_{10}^{\bullet+}$ displays cross-peaks that arise from the electron-nuclear hyperfine interactions of the unpaired electron spin with the nitrogen-14 atoms (nuclear spin, I = 1) of the BiP and PF_{10} moieties (Figure 4A). The position of the cross-peaks in the spectrum is determined by the Zeeman frequency of the ^{14}N atoms arising from the nuclear magnetic interaction (ν_I^N of 1.06 MHz) and the electron-nuclear hyperfine interaction, A. In the strong coupling limit (when $A > 2\nu_I^N$), the cross-peaks appear in the (–,+) quadrant, while in the weak coupling limit (when $A < 2\nu_I^N$) the cross-peaks are in the (+,+) quadrant of the spectrum (Höfer et al., 1986; Schweiger and Jeschke, 2001).

Accordingly, the (–,+) quadrant of the 2D ^{14}N spectrum of BiP–$PF_{10}^{\bullet+}$ in Figure 4A displays three sets of cross-peaks that are symmetric about the anti-diagonal. The origin of these peaks are the nitrogen atoms, N^I–N^{III}, that are strongly hyperfine coupled to the unpaired electron spin. In each case, the shift along the diagonal from multiples of the ^{14}N Zeeman frequency, ν_I^N (shown as dashed red lines in Figure 4A), is due to the quadrupolar interaction of the nitrogen atoms, whereas the separation of the cross-peaks along the anti-diagonal is due to the hyperfine interaction with the unpaired electron spin. In contrast, the (+,+) quadrant of the 2D ^{14}N HYSCORE spectrum in Figure 4A displays cross-peaks that arise from the weakly hyperfine coupled nitrogen atoms, N^{IV}–N^{VI}. The two closely located cross-peaks in the (+,+) quadrant of the spectrum that are symmetric with respect to the diagonal are assigned to the double quantum transitions of the weakly coupled nitrogen atoms, N^{IV}–N^{V}. In contrast, the absence of resolved structure of the cross-peak along the diagonal indicates that the nitrogen atom, N^{VI}, is very weakly hyperfine coupled to the unpaired electron spin. Additionally, although the cross-peaks from the N^I nitrogen atom appear in only in the (–,+) quadrant, the cross-peaks arising from N^{II} are also present in the (+,+) quadrant (as labeled in Figures 4A and 4B).

The principal values of the spin Hamiltonian parameters of all of the contributing hyperfine coupled ^{14}N atoms can be determined by numerical simulations to obtain a best fit of the cross-peaks in the experimental 2D ^{14}N HYSCORE spectrum (Figure 4B). The simulations provide an accurate determination of isotropic hyperfine coupling, A_{iso}, as well as the value of $K^2(3 + \eta^2)$, where the quadrupolar coupling constant, $K = e^2qQ/4\hbar$, Q is the quadrupole moment interacting with the electric field gradient q, and η is the asymmetry parameter, for each nitrogen atom that is magnetically coupled to the unpaired electron spin (Table 1). In the (–,+) quadrant of the 2D HYSCORE spectrum in Figure 4A, the most intense cross-peaks from the nitrogen atoms, N^I and N^{II}, are overlapping at ($\mp$ 2.6, $\pm$1.3) MHz. This is because N^I and N^{II} possess similar magnetic parameters, namely, $K = -0.60$ MHz, $\eta = 0.50$, and $A_{iso} = 1.12$ MHz for N^I and $K = -0.58$ MHz, $\eta = 0.52$, and $A_{iso} = 1.05$ MHz for N^{II}. Based on the values of K of −0.60 to −0.58 MHz and η of 0.50–0.52, we assigned N^I and N^{II} to the nitrogen atoms of the benzimidazole moiety, BiP. The

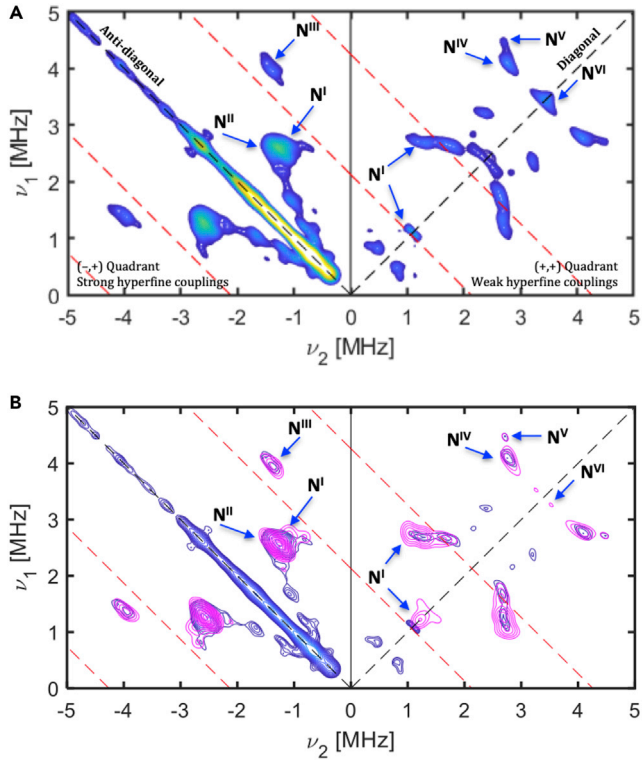

Figure 4. 2D ^{14}N HYSCORE Spectra of the PCET Radical Intermediate of Benzimidazole Phenol Porphyrin, BiP-PF$_{10}$

The (A) experimental and (B) simulated 2D ^{14}N HYSCORE spectrum of BiP–PF$_{10}^{\bullet+}$ radical. The (-,+) quadrant displays cross-peaks from the strong hyperfine couplings of the electron spin with three nitrogen atoms, N^{I}–N^{III}, that are symmetric about the anti-diagonal. In contrast, the (+,+) quadrant contains cross-peaks from weaker hyperfine couplings with the N^{IV}–N^{VI} nitrogen atoms that are symmetric with respect to the diagonal. The dashed red lines in (A) and (B) indicate multiples of the ^{14}N Zeeman frequency, ν_I^N, of 1.06 MHz.

assignment is based on previous nuclear quadrupole resonance (NQR) studies that have demonstrated that the quadrupolar coupling constant ($e^2qQ/\hbar$) for the amino nitrogen atom of an imidazole side chain is ~1.4–2.4 MHz (Edmonds, 1977). The position of the cross-peaks due to N^{I} and N^{II} is determined by the value of A_{iso}, whereas the anisotropy manifests itself as second-order effects. As mentioned earlier, the cross-peaks display observable shifts from the nuclear Zeeman frequency (shown as dashed red lines in Figure 4B) due to the influence of the *K* values. There is also a third set of cross-peaks located at ($\mp$ 3.9, $\pm$1.3) MHz in the (−,+) quadrant that arise from a hyperfine interaction of the unpaired electron spin with the nitrogen atom, N^{III}, with a *K* of −0.66 MHz that is strongly coupled to the electron spin ($A > 2\nu_I$) (Table 1). Based on the value of *K* of −0.66 MHz, we assigned N^{III} to a pyrrole nitrogen in the PF$_{10}$ ring (Charles et al., 2020; García-Rubio et al., 2003).

In the (+,+) quadrant of the 2D HYSCORE spectrum in Figures 4A and 4B, there are two pairs of resolved cross-peaks separated from the diagonal points centered at (3.3, 3.3) MHz, which arise from weak hyperfine interactions of the unpaired electron spin with the nitrogen atoms, N^{IV} and N^{V}. The separation of the cross-peaks along the anti-diagonal corresponds to the weak coupling regime $A < 2\nu_I$ and hence the peaks are located in a frequency region closer to the diagonal. Finally, the cross-peak arising from the weakest hyperfine interaction with the nitrogen atom, N^{VI}, with the smallest A_{iso} value is located along the diagonal. The *K* values of all three nitrogen atoms, N^{IV}–N^{VI}, are in the range of −0.69 to −0.72 MHz, which is comparable with the *K* values that have previously been observed for pyrrole nitrogen atoms of a porphyrin ring (Charles et al., 2020; García-Rubio et al., 2003). Thus, we assign N^{IV}–N^{VI} to the remaining pyrrole nitrogen atoms in the PF$_{10}$ moiety.

It is notable that the porphyrin nitrogen atom, N^{III}, displays a strong isotropic hyperfine coupling, A_{iso}, of 2.15 MHz, which indicates the presence of significant electron spin density at this location. In comparison,

Nitrogen	K (MHz) (Experimental)	A_{iso} (MHz) (Experimental)	K (MHz) (Calculated C Structure)	A_{iso} (MHz) (Calculated C Structure)
N^{I}	−0.59 ± 0.01	1.05 ± 0.1	−0.66	1.17
N^{II}	−0.60 ± 0.02	1.12 ± 0.1	−0.58	0.88
N^{III}	−0.66 ± 0.01	2.15 ± 0.1	−0.80	2.21
N^{IV}	−0.72 ± 0.01	0.50 ± 0.1	−0.75	0.41
N^{V}	−0.70 ± 0.01	0.40 ± 0.2	−0.75	0.77
N^{VI}	−0.69 ± 0.01	−0.20 ± 0.1	−0.80	−0.18

Table 1. The ^{14}N Hyperfine and Quadrupolar Parameters that Are Obtained from Spectral Simulations of the Experimental 2D ^{14}N HYSCORE Spectrum of the BiP–$PF_{10}^{\bullet+}$ and DFT Calculations of the C Structure of the BiP–$PF_{10}^{\bullet+}$

the remaining nitrogen atoms of the porphyrin ring, N^{IV}–N^{VI}, display relatively small values of isotropic hyperfine coupling constant of −0.2 to 0.5 MHz. The observation of finite isotropic hyperfine coupling constants, A_{iso}, for all of the nitrogen atoms, N^{I}–N^{VI}, clearly indicates that the electron spin density is delocalized on both the benzimidazole phenol, BiP, and high-potential porphyrin, PF_{10}, in BiP–$PF_{10}^{\bullet+}$.

The A_{iso} values of 1.05 and 1.12 MHz for the nitrogen atoms, N^{I} and N^{II}, of BiP indicates that the magnitude of electron spin density that is distributed on the two nitrogen atoms is comparable. Typically, the A_{iso} values are determined by the unpaired spin density in the 2*s* orbital that is proportional to atomic value of 1,811 MHz for ^{14}N, computed for unit spin density in this orbital (Morton and Preston, 1978). Therefore, the A_{iso} value of 1.05–1.12 MHz that is determined for the N^{I} and N^{II} nitrogen atoms of BiP corresponds to a fractional spin density distribution, ρ_s, of $\approx 6.0\times10^{-4}$ in the 2*s* orbital of each nitrogen atom. This suggests that the strength of the H-bonds between each nitrogen atom of BiP and its proximal water molecule are nearly equivalent. Moreover, the values of the isotropic hyperfine coupling constant, A_{iso}, indicate the presence of significant spin density on the strongly coupled nitrogen atom, N^{III}, of the porphyrin ring, PF_{10}, along with a smaller fraction of spin density on the three weakly coupled nitrogen atoms, N^{IV}–N^{VI}. The PF_{10} molecule is an aromatic ring system; therefore, the π-electron density is delocalized over the nitrogen atoms of the PF_{10} ring. The relative differences in A_{iso} values reflect differences in the distribution of spin density on the nitrogen atoms, N^{IV}–N^{VI}, of the porphyrin ring (Table 1).

We performed DFT calculations (see Transparent Methods) on three computational models (**A**, **B**, and **C**) shown in Figures 5A–5C (and Figures S1–S3), respectively, to elucidate the high-resolution electronic structure of BiP–$PF_{10}^{\bullet+}$ and understand the role that water molecules play in the PCET process. All three structures correspond to the chemical species that would result from the transfer of the proton from the phenolic oxygen atom to the proximal imidazole nitrogen atom of BiP during PCET, thus resulting in a BiP–$PF_{10}^{\bullet+}$. Model **A** does not include any water molecules (Figure 5A), whereas the models **B** and **C** include explicit water molecules that are H-bonded to the BiP moiety of the BiP–$PF_{10}^{\bullet+}$ radical (Figures 5B and 5C). The structure of **B** (Figure 5B) includes two explicit water molecules, one water molecule that forms an H-bond with the distal N–H of BiP and another that forms an H-bond to the phenoxyl oxygen atom. The alternate structure, **C**, also contains two water molecules, where one water acts as an H-bond acceptor to the distal amino N–H of BiP and a second water molecule serves as both a H-bond acceptor and donor to the newly formed N–H and phenoxyl oxygen atom, respectively (Figure 5C).

The DFT calculations allow for a comparison of the electron spin density distribution in each of the computational models, **A**, **B**, and **C** (Figures 6A–6C, respectively). Although the electron spin density is distributed on the imidazole and phenol of the BiP moiety in all three models, we also observe delocalization of the unpaired electron spin onto the conjugated porphyrin, PF_{10}. The delocalization of the electron spin on both BiP and PF_{10} in these structures is in agreement with the experimental 2D ^{14}N HYSCORE measurements where we observe hyperfine interactions of the unpaired electron with the nitrogen atoms of both BiP (N^{I} and N^{II}) and PF_{10} (N^{III}–N^{VI}) (Figures 4A and 4B and Table 1). The delocalization of the electron

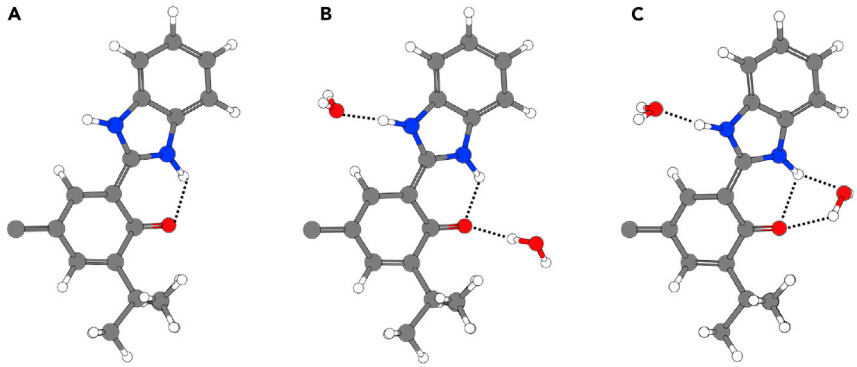

Figure 5. DFT Structures of Benzimidazole Phenol Porphyrin, BiP-PF_{10}

The DFT optimized structure of the BiP moiety in the **A**, **B**, and **C** structure of the BiP–$PF_{10}$$^{\bullet+}$, where PF_{10} is omitted for clarity. Both structures **B** and **C** contain two water molecules but differ in the H-bonding pattern between the phenolic O atom, imidazole nitrogen atom, and proximal water molecule. In contrast, structure **A** does not contain any water molecules.

spin density is also consistent with previous theoretical analysis on the methyl ester derivative of BiP–PF_{10} (Huynh et al., 2017; Megiatto et al., 2014).

In addition to obtaining the electron spin density distribution of the structures, we calculated the quadrupolar and hyperfine parameters (*K* and A_{iso}, respectively) for comparison with the experimental values that were obtained from the 2D ^{14}N HYSCORE measurements. The calculated *K* values that are obtained for all of the nitrogen atoms, N^{I}–N^{VI}, for the **A**, **B**, and **C** structures are comparable with the *K* values that are determined from the 2D HYSCORE measurements. In particular, the value of *K* for the benzimidazole (N^{I}–N^{II}) and porphyrin (N^{III}–N^{VI}) nitrogen atoms of the **C** structure was 0.62 $\pm$ 0.04 and 0.77 $\pm$ 0.03 MHz, respectively (Table 1). This is in agreement with the experimental values of *K* for the BiP and PF_{10} nitrogen atoms, within an average error of 0.07 MHz.

The calculated value of the isotropic hyperfine coupling constant, A_{iso}, that is obtained for the benzimidazole nitrogens, N^{I} and N^{II}, in the **C** structure was 1.17 and 0.88 MHz, respectively, whereas the corresponding value for the porphyrin nitrogens, N^{III}–N^{VI}, was 2.2, 0.41, 0.77, and −0.17 MHz, respectively. The calculated values for A_{iso} are in agreement with the experimental couplings of N^{I}–N^{VI}; the average error was 0.15 MHz. In contrast, the average error for the calculated values A_{iso} for **B** and **A** structures was 0.52 and 0.33 MHz, respectively (as shown in Tables S1 and S2).

The corresponding **g**-tensors that are obtained from the DFT calculations of the **A**, **B**, and **C** structures are presented in Table S3. Previous high-frequency EPR and ENDOR measurements on the redox-active tyrosine-D radical of photosystem II (Chatterjee et al., 2013; Faller et al., 2002; Un et al., 1996, 1994) and TiO_2–PF_{10}BiP triad (Megiatto et al., 2014) have demonstrated that the g_X component of the **g**-tensor for a tyrosyl radical that is oriented along the C-O molecular axis is sensitive to the local environment of the phenolic oxygen atom. In this case, the spin-orbit coupling interaction between the unpaired electron in the singly occupied molecular orbital (SOMO) and the lone pairs of electrons on the phenolic oxygen atom induce a magnetic moment that results in a rather large deviation of the g_X component of the **g**-tensor (e.g., g_X of ~2.008) from the free electron g-value (g_e = 2.0023) (Megiatto et al., 2014; Stone, 1963). However, the presence of H-bonding interaction(s) with the lone pair on the phenolic oxygen atom and/or delocalization of the unpaired spin density tend to decrease this deviation, yielding radicals with lower g_X values (Chatterjee et al., 2013; Faller et al., 2002; Retegan et al., 2014; Un et al., 1996, 1994). This is in agreement with the g_X component of the **g**-tensor of 2.0056, 2.0052, and 2.0061 that is calculated for the **A**, **B**, and **C** structures (Table S3). The g_X component that was observed for the **A**, **B**, and **C** structures is lower than the calculated g_X value of ~2.0065 that was obtained for a series of phenoxyl radicals that were H-bonded to a imidazolium moiety in the absence of a covalently linked conjugated system (Benisvy et al., 2005). Similarly, the g_X component of the **A**, **B**, and **C** structures is also less than the g_X value of 2.0065 that was previously reported for a BiP–PF_{10} derivative in which the porphyrin molecule was covalently bonded to BiP through the imidazole moiety instead of the phenol, which precluded delocalization of the electron spin density between the BiP and PF_{10} moieties (Moore et al., 2010). Hence, in the present study the smaller

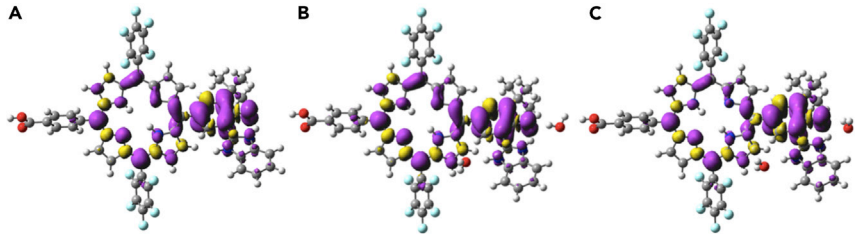

Figure 6. Electron Spin Density Distribution in the DFT Structures of the PCET Radical Intermediates of Benzimidazole Phenol Porphyrin, BiP-PF_{10}

The electron spin density (purple and gold) distribution of the **A**, **B**, and **C** structures of BiP–$PF_{10}^{\bullet+}$ as determined by DFT. The atoms are color coded as carbon (gray), hydrogen (white), nitrogen (blue), fluorine (cyan), and oxygen (red). The spin population ratio (PF_{10}:BiP) is 35:65, 35:65, and 20:80 for structures **A**, **B**, and **C**, respectively.

value of 2.0056, 2.0052, and 2.0061 that is obtained for the g_X component of the **A**, **B**, and **C** structure is attributed to the effects from the strong H-bonding interactions at the phenoxyl oxygen atom and to a lesser degree the delocalization of the electron spin density on both BiP and PF_{10}.

In our previous work, we had demonstrated that calculated g-values for structure **B** were in better agreement with the corresponding experimental values of the radical species obtained by illumination at 13 K (prior to annealing the sample at 77 K). In contrast, the calculated g-values for structure **C** were in better agreement with those of the radical after annealing the sample at 77 K (Megiatto et al., 2014). We had rationalized this with the fact that, before PCET the nitrogen of the imidazole that is H-bonded to the phenol is a hydrogen bond acceptor, but after PCET the nitrogen accepts the phenolic proton forming an N–H group and is therefore a hydrogen bond donor. The PCET reactions occur at 13 K but lack the thermal energy for solvent reorganization and form an H-bond with the newly formed N–H group (structure **B**). Once the sample is annealed, the solvent is able to reorganize and form a bifurcated H-bond between the newly formed N–H and the phenolic oxygen atom (structure **C**). This indicates that, in the present study the illumination of BiP–PF_{10} with white light at 77 K should lead to the formation of a cation radical whereby upon PCET, the nitrogen atom of BiP accepts the phenolic proton resulting in an N–H that is in a bifurcated H-bond.

Based on the magnetic parameters of the computational models of BiP–PF_{10}, **A**, **B**, and **C**, we examine the geometric parameters and relative energies of the DFT structures. We find that the extent of electron spin delocalization between BiP and PF_{10} in the three DFT structures (Figures 6A–6C) can be explained in terms of the dihedral angle between the conjugated rings of BiP and PF_{10}. The delocalization of the electron on BiP and PF_{10} is greater when the dihedral angle between the planes of the BiP and PF_{10} ring tends to 0° and is diminished when the dihedral angle tends to 90° (i.e., when the rings are orthogonal). As observed in Table 2, the dihedral angle between the BiP and PF_{10} is ~47° for all of the structures.

The main structural difference between the computational models is the dihedral angle between the benzimidazole and phenolic group of BiP. As shown in Table 2, the BiP system is almost co-planar for the **A** and **B** structures, but it is twisted slightly out of plane for **C** structure (with a dihedral angle of ~7°). We hypothesize that this difference is caused by the relaxation of the water molecules around the newly formed N–H bond, which forms a bifurcated H-bond with both the phenolic and water oxygen atoms thus lowering the strength of the intra-molecular hydrogen bond. The effects of the spin density delocalization can be also observed in the A_{iso} values for specific nitrogen within the different structures. The deviation of the experimental and calculated A_{iso} value for N^{II} is 0.24, 0.67, and 0.55 MHz for models **C**, **B**, and **A**, respectively. The deviation of the experimental and calculated A_{iso} value for N^{III} is 0.06, 0.85, and 0.30 MHz for models **C**, **B**, and **A**, respectively. These results highlight the importance of incorporating explicit water molecules in the models in the right conformation. Finally, as shown in Table 2, the energy of structure **C** is ~3 kcal/mol lower than the energy of structure **B**. Therefore, the relaxation from structure **B** to structure **C** is thermodynamically favorable, which is consistent with the discussion above.

Conclusions

In the present study, we determine the experimental and calculated electron spin density distribution on the radical species that is formed upon light-induced PCET in the artificial reaction center, BiP–PF_{10}. We demonstrate excellent agreement between the hyperfine coupling constants of the nitrogen atoms that are determined by experimental 2D ^{14}N HYSCORE spectroscopy and those calculated by DFT methods. Moreover, we observe

Structure	Benzimidazole-Phenol Dihedral Angle	BiP–Porphyrin Dihedral Angle	ΔE Relative to Structure A (kcal/mol)
A	1.7	48.5	Reference
B	1.8	44.5	−16.2
C	7.1	47.6	−19.1

Table 2. The Relative Energies (ΔE) and Relevant Dihedral Angles of the A, B and C Structure of BiP–$PF_{10}^{\cdot+}$ that Were Optimized by DFT Calculations

that there is a direct correlation between the hyperfine coupling constants of the nitrogen atoms and delocalization of electron spin density in the presence and absence of structural water molecules in the vicinity of the BiP and porphyrin moieties of BiP–PF_{10}. The presence of two explicit water molecules in the **C** structure that are hydrogen bonded to the N–H sites of the BiP moiety leads to a near perfect match of the experimental and calculated hyperfine couplings. This highlights the importance of hydrogen bonding interactions with water molecules in the favorable tuning of the electronic structure and respective energy levels that facilitates PCET reactions in the BiP–PF_{10} reaction center. In contrast, the experimental hyperfine coupling constants are not as well reproduced in the related structures, **A** and **B**, that exhibit differences in the hydrogen bonding pattern or a complete absence of such interactions with structured water molecules. These results present direct experimental and theoretical evidence of spin delocalization and highlights the effects of structured water molecules on the tuning of the electronic structure of artificial reaction centers. The results of this study emphasize the importance of considering these factors in the experimental and computational design of novel artificial photosynthetic systems that incorporate multi-electron and PCET processes.

Limitations of the Study

One limitation of the model system in this study is that it lacks the moieties necessary to simulate the amino acid environment surrounding the distal N–H of the BiP as has been implemented in other studies (Huynh et al., 2017; Odella et al., 2019, 2018).

Resources Availability

Lead Contact

Further information and requests for resources should be directed to and will be fulfilled by the Lead Contact, Dalvin D. Méndez-Hernández (dalvin.mendez@upr.edu).

Materials Availability

This study did not generate new unique reagents.

Data and Code Availability

The published article includes all datasets generated or analyzed during this study. This study did not generate new code.

METHODS

All methods can be found in the accompanying Transparent Methods supplemental file.

SUPPLEMENTAL INFORMATION

Supplemental Information can be found online at https://doi.org/10.1016/j.isci.2020.101366.

ACKNOWLEDGMENTS

This study was supported by the Department of Energy, Office of Science, Office of Basic Energy Sciences, under Awards DE-FG02-07ER15903 (K.V.L., Photosynthetic Systems Program), and DE-FG02-03ER15393 (A.L.M and T.A.M.). The computational resources at Rensselaer were provided by the Center for Computational Innovations (CCI). D.D.M.-H was supported by the Start-Up funds and the "Fondo Institucional para el Desarrollo de la Investigación (FIDI)" of the University of Puerto Rico at Cayey. Computational resources were provided in part by the High-Performance Computing Facility at the University of Puerto Rico

supported by the Institutional Development Award (IDeA) INBRE Grant Number P20GM103475 from the National Institute of General Medical Sciences (NIGMS), a component of the National Institutes of Health (NIH) and the Bioinformatics Research Core of INBRE. Its contents are solely the responsibility of the authors and do not necessarily represent the official view of NIGMS or NIH. The authors would like to thank Oleg G. Poluektov (ANL) for helpful discussions.

AUTHOR CONTRIBUTIONS

D.D.M.-H., A.B., V.K., P.C., B. Mark, W.M., and B. Molnar conducted experiments, analyzed the data, and performed calculations; D.D.M.-H., K.V.L., A.L.M., and T.A.M. designed the experiments and wrote the paper.

DECLARATION OF INTERESTS

The authors declare no competing interests.

Received: May 17, 2020
Revised: June 22, 2020
Accepted: July 10, 2020
Published: August 21, 2020

REFERENCES

Ahlbrink, R., Haumann, M., Cherepanov, D., Bögershausen, O., Mulkidjanian, A., and Junge, W. (1998). Function of tyrosine Z in water oxidation by photosystem II: electrostatical promotor instead of hydrogen abstractor. Biochemistry *37*, 1131–1142.

Barber, J. (2008). Photosynthetic energy conversion: natural and artificial. Chem. Soc. Rev. *38*, 185–196.

Barry, B.A., el-Deeb, M.K., Sandusky, P.O., and Babcock, G.T. (1990). Tyrosine radicals in photosystem II and related model compounds. Characterization by isotopic labeling and EPR spectroscopy. J. Biol. Chem. *265*, 20139–20143.

Barry, B.A., Brahmachari, U., and Guo, Z. (2017). Tracking reactive water and hydrogen-bonding networks in photosynthetic oxygen evolution. Acc. Chem. Res. *50*, 1937–1945.

Benisvy, L., Bittl, R., Bothe, E., Garner, C.D., McMaster, J., Ross, S., Teutloff, C., and Neese, F. (2005). Phenoxyl radicals hydrogen-bonded to imidazolium: analogues of tyrosyl D. of photosystem II: high-field EPR and DFT studies. Angew. Chem. Int. Ed. *117*, 5448–5451.

Berthomieu, C., and Hienerwadel, R. (2005). Vibrational spectroscopy to study the properties of redox-active tyrosines in photosystem II and other proteins. Biochim. Biophys. Acta *1707*, 51–66.

Britt, R.D. (2003). Electron spin echo methods: a tutorial. In Paramagnetic Resonance of Metallobiomolecules, ACS Symposium Series, J. Telser, ed. (American Chemical Society), pp. 16–54.

Chai, J., Zheng, Z., Pan, H., Zhang, S., Lakshmi, K.V., and Sun, Y.-Y. (2019). Significance of hydrogen bonding networks in the proton-coupled electron transfer reactions of photosystem II from a quantum-mechanics perspective. Phys. Chem. Chem. Phys. *21*, 8721–8728.

Charles, P., Kalendra, V., He, Z., Khatami, M.H., Golbeck, J.H., van der Est, A., Lakshmi, K.V., and Bryant, D.A. (2020). Two-dimensional ^{67}Zn HYSCORE spectroscopy reveals that a Zn-bacteriochlorophyll a_P' dimer is the primary donor (P_{840}) in the type-1 reaction centers of *Chloracidobacterium thermophilum*. Phys. Chem. Chem. Phys. *22*, 6457–6467.

Chatterjee, R., Milikisiyants, S., and Lakshmi, K.V. (2012). Two-dimensional ^{14}N HYSCORE spectroscopy of the coordination geometry of ligands in dimanganese di-μ-oxo mimics of the oxygen-evolving complex of photosystem II. Phys. Chem. Chem. Phys. *14*, 7090–7097.

Chatterjee, R., Coates, C.S., Milikisiyants, S., Lee, C.-I., Wagner, A., Poluektov, O.G., and Lakshmi, K.V. (2013). High-frequency electron nuclear double resonance spectroscopy studies of the mechanism of proton-coupled electron transfer at the tyrosine-D residue of photosystem II. Biochemistry *52*, 4781–4790.

Christen, G., Seeliger, A., and Renger, G. (1999). $P_{680}^{+\bullet}$ reduction kinetics and redox transition probability of the water oxidizing complex as a function of pH and H/D isotope exchange in spinach thylakoids. Biochemistry *38*, 6082–6092.

Chrysina, M., de Mendonça Silva, J.C., Zahariou, G., Pantazis, D.A., and Ioannidis, N. (2019). Proton translocation via tautomerization of Asn298 during the S_2–S_3 state transition in the oxygen-evolving complex of photosystem II. J. Phys. Chem. B *123*, 3068–3078.

Coates, C.S., Milikisiyants, S., Chatterjee, R., Whittaker, M.M., Whittaker, J.W., and Lakshmi, K.V. (2015). Two-dimensional HYSCORE spectroscopy of superoxidized manganese catalase: a model for the oxygen-evolving complex of photosystem II. J. Phys. Chem. B *119*, 4905–4916.

Cukier, R.I., and Nocera, D.G. (1998). Proton-coupled electron transfer. Annu. Rev. Phys. Chem. *49*, 337–369.

Debus, R.J. (1992). The manganese and calcium ions of photosynthetic oxygen evolution. Biochim. Biophys. Acta *1102*, 269–352.

Deligiannakis, Y., Louloudi, M., and Hadjiliadis, N. (2000). Electron spin echo envelope modulation (ESEEM) spectroscopy as a tool to investigate the coordination environment of metal centers. Coord. Chem. Rev. *204*, 1–112.

Dikanov, S.A., and Taguchi, A.T. (2018). Two-dimensional pulsed EPR resolves hyperfine coupling strain in nitrogen hydrogen bond donors of semiquinone intermediates. J. Phys. Chem. B *122*, 5205–5211.

Dikanov, S.A., Tyryshkin, A.M., and Bowman, M.K. (2000). Intensity of cross-peaks in HYSCORE spectra of S = 1/2, I = 1/2 spin systems. J. Magn. Reson. *144*, 228–242.

Dikanov, S.A., Berry, S.M., and Lu, Y. (2019). HYSCORE insights into the distribution of the unpaired spin density in an engineered Cu_A site in azurin and its His120Gly variant. Inorg. Chem. *58*, 4437–4445.

Diner, B.A., and Rappaport, F. (2002). Structure, dynamics, and energetics of the primary photochemistry of photosystem II of oxygenic photosynthesis. Annu. Rev. Plant Biol. *53*, 551–580.

Edmonds, D.T. (1977). Nuclear quadrupole double resonance. Phys. Rep. *29*, 233–290.

Faller, P., Rutherford, A.W., and Debus, R.J. (2002). Tyrosine D oxidation at cryogenic temperature in photosystem II. Biochemistry *41*, 12914–12920.

García-Rubio, I., Martínez, J.I., Picorel, R., Yruela, I., and Alonso, P.J. (2003). HYSCORE spectroscopy in the cytochrome b_{559} of the photosystem II reaction center. J. Am. Chem. Soc. *125*, 15846–15854.

Gasyna, Z., Browett, W.R., and Stillman, M.J. (1984). One-electron photooxidation of

porphyrins at low temperature. Inorg. Chim. Acta *92*, 37–42.

Gust, D., Moore, T.A., and Moore, A.L. (2009). Solar fuels via artificial photosynthesis. Acc. Chem. Res. *42*, 1890–1898.

Hadt, R.G., Hayes, D., Brodsky, C.N., Ullman, A.M., Casa, D.M., Upton, M.H., Nocera, D.G., and Chen, L.X. (2016). X-ray spectroscopic characterization of Co(IV) and metal–metal interactions in Co_4O_4: electronic structure contributions to the formation of high-valent states relevant to the oxygen evolution reaction. J. Am. Chem. Soc. *138*, 11017–11030.

Harbour, J.R., and Tollin, G. (1974). Chlorophyll one-electron photochemistry-I. Photoproduction of the cation radicals of chlorophyll and bacteriochlorophyll in solutions at low temperatures. Photochem. Photobiol. *19*, 69–74.

Harmer, J., Mitrikas, G., and Schweiger, A. (2009). Advanced pulse EPR methods for the characterization of metalloproteins. In High Resolution EPR, G. Hanson and L. Berliner, eds. (Springer), pp. 13–61.

Hart, R., and O'Malley, P.J. (2010). A quantum mechanics/molecular mechanics study of the tyrosine residue, Tyr_D, of photosystem II. Biochim. Biophys. Acta *1797*, 250–254.

Höfer, P., Grupp, A., Nebenführ, H., and Mehring, M. (1986). Hyperfine sublevel correlation (HYSCORE) spectroscopy: a 2D ESR investigation of the squaric acid radical. Chem. Phys. Lett. *132*, 279–282.

Hoganson, C.W., and Babcock, G.T. (1997). A metalloradical mechanism for the generation of oxygen from water in photosynthesis. Science *277*, 1953–1956.

Hoganson, C.W., and Tommos, C. (2004). The function and characteristics of tyrosyl radical cofactors. Biochim. Biophys. Acta *1655*, 116–122.

Huynh, M.T., Mora, S.J., Villalba, M., Tejeda-Ferrari, M.E., Liddell, P.A., Cherry, B.R., Teillout, A.-L., Machan, C.W., Kubiak, C.P., Gust, D., et al. (2017). Concerted one-electron two-proton transfer processes in models inspired by the Tyr-His couple of photosystem II. ACS Cent. Sci. *3*, 372–380.

Ishikita, H., and Knapp, E.-W. (2006). Function of redox-active tyrosine in photosystem II. Biophys. J. *90*, 3886–3896.

Jenson, D.L., Evans, A., and Barry, B.A. (2007). Proton-coupled electron transfer and tyrosine D of photosystem II. J. Phys. Chem. B *111*, 12599–12604.

Kawashima, K., Saito, K., and Ishikita, H. (2018). Mechanism of radical formation in the H-bond network of D1-Asn298 in photosystem II. Biochemistry *57*, 4997–5004.

Keßen, S., Teutloff, C., Kern, J., Zouni, A., and Bittl, R. (2010). High-field ^{2}H mims-ENDOR spectroscopy on PSII single crystals: hydrogen bonding of Y_D. Chem. Phys. Chem. *11*, 1275–1282.

Lakshmi, K.V., and Brudvig, G.W. (2001). Pulsed electron paramagnetic resonance methods for macromolecular structure determination. Curr. Opin. Struct. Biol. *11*, 523–531.

Linschitz, H., and Rennert, J. (1952). Reversible photo-bleaching of chlorophyll in rigid solvents. Nature *169*, 193–194.

Livingston, R., and Ryan, V.A. (1953). The phototropy of chlorophyll in fluid Solutions1,2. J. Am. Chem. Soc. *75*, 2176–2181.

Maayan, G., Gluz, N., and Christou, G. (2018). A bioinspired soluble manganese cluster as a water oxidation electrocatalyst with low overpotential. Nat. Catal. *1*, 48.

McEvoy, J.P., and Brudvig, G.W. (2004). Structure-based mechanism of photosynthetic water oxidation. Phys. Chem. Chem. Phys. *6*, 4754–4763.

McEvoy, J.P., and Brudvig, G.W. (2006). Water-splitting chemistry of photosystem II. Chem. Rev. *106*, 4455–4483.

Megiatto, J.D., Jr., Méndez-Hernández, D.D., Tejeda-Ferrari, M.E., Teillout, A.-L., Llansola-Portolés, M.J., Kodis, G., Poluektov, O.G., Rajh, T., Mujica, V., Groy, T.L., et al. (2014). A bioinspired redox relay that mimics radical interactions of the Tyr–His pairs of photosystem II. Nat. Chem. *6*, 423–428.

Meot-Ner, M. (2005). The ionic hydrogen bond. Chem. Rev. *105*, 213–284.

Milikisiyants, S., Chatterjee, R., Weyers, A., Meenaghan, A., Coates, C., and Lakshmi, K.V. (2010). Ligand environment of the S_2 state of photosystem II: a study of the hyperfine interactions of the tetranuclear manganese cluster by 2D ^{14}N HYSCORE spectroscopy. J. Phys. Chem. B *114*, 10905–10911.

Milikisiyants, S., Chatterjee, R., and Lakshmi, K.V. (2011). Two-dimensional ^{1}H HYSCORE spectroscopy of dimanganese Di-μ-oxo mimics of the oxygen-evolving complex of photosystem II. J. Phys. Chem. B *115*, 12220–12229.

Moore, G.F., Hambourger, M., Kodis, G., Michl, W., Gust, D., Moore, T.A., and Moore, A.L. (2010). Effects of protonation state on a Tyrosine−Histidine bioinspired redox mediator. J. Phys. Chem. B *114*, 14450–14457.

Morton, J.R., and Preston, K.F. (1978). Atomic parameters for paramagnetic resonance data. J. Magn. Reson. *30*, 577–582.

Odella, E., Mora, S.J., Wadsworth, B.L., Huynh, M.T., Goings, J.J., Liddell, P.A., Groy, T.L., Gervaldo, M., Sereno, L.E., Gust, D., et al. (2018). Controlling proton-coupled electron transfer in bioinspired artificial photosynthetic relays. J. Am. Chem. Soc. *140*, 15450–15460.

Odella, E., Wadsworth, B.L., Mora, S.J., Goings, J.J., Huynh, M.T., Gust, D., Moore, T.A., Moore, G.F., Hammes-Schiffer, S., and Moore, A.L. (2019). Proton-coupled electron transfer drives long-range proton translocation in bioinspired systems. J. Am. Chem. Soc. *141*, 14057–14061.

Osterloh, F.E. (2008). Inorganic materials as catalysts for photochemical splitting of water. Chem. Mater. *20*, 35–54.

Prisner, T., Rohrer, M., and MacMillan, F. (2001). Pulsed EPR spectroscopy: biological applications. Annu. Rev. Phys. Chem. *52*, 279–313.

Retegan, M., Cox, N., Lubitz, W., Neese, F., and Pantazis, D.A. (2014). The first tyrosyl radical intermediate formed in the S_2–S_3 transition of photosystem II. Phys. Chem. Chem. Phys. *16*, 11901–11910.

Romero, E., Novoderezhkin, V.I., and van Grondelle, R. (2017). Quantum design of photosynthesis for bio-inspired solar-energy conversion. Nature *543*, 355–365.

Rutherford, A.W., Boussac, A., and Faller, P. (2004). The stable tyrosyl radical in photosystem II: why D? Biochim. Biophys. Acta *1655*, 222–230.

Saito, K., Shen, J.-R., Ishida, T., and Ishikita, H. (2011). Short hydrogen bond between redox-active tyrosine Y_Z and D1-His190 in the photosystem II crystal structure. Biochemistry *50*, 9836–9844.

Saito, K., Rutherford, A.W., and Ishikita, H. (2013). Mechanism of tyrosine D oxidation in photosystem II. Proc. Natl. Acad. Sci. U S A *110*, 7690–7695.

Saito, K., Sakashita, N., and Ishikita, H. (2016). Energetics of the proton transfer pathway for tyrosine D in photosystem II. Aust. J. Chem. *69*, 991–998.

Sakamoto, H., Shimizu, T., Nagao, R., and Noguchi, T. (2017). Monitoring the reaction process during the $S_2 \rightarrow S_3$ transition in photosynthetic water oxidation using time-resolved infrared spectroscopy. J. Am. Chem. Soc. *139*, 2022–2029.

Sakashita, N., Watanabe, H.C., Ikeda, T., Saito, K., and Ishikita, H. (2017). Origins of water molecules in the photosystem II crystal structure. Biochemistry *56*, 3049–3057.

Schweiger, A., and Jeschke, G. (2001). Principles of Pulse Electron Paramagnetic Resonance (Oxford University Press on Demand).

Shen, J.-R. (2015). The structure of photosystem II and the mechanism of water oxidation in photosynthesis. Annu. Rev. Plant Biol. *66*, 23–48.

Sirohiwal, A., Neese, F., and Pantazis, D.A. (2019). Microsolvation of the redox-active tyrosine-D in photosystem II: correlation of energetics with EPR spectroscopy and oxidation-induced proton transfer. J. Am. Chem. Soc. *141*, 3217–3231.

Sokol, K.P., Robinson, W.E., Warnan, J., Kornienko, N., Nowaczyk, M.M., Ruff, A., Zhang, J.Z., and Reisner, E. (2018). Bias-free photoelectrochemical water splitting with photosystem II on a dye-sensitized photoanode wired to hydrogenase. Nat. Energy *3*, 944.

Stone, A.J. (1963). g factors of aromatic free radicals. Mol. Phys. *6*, 509–515.

Styring, S., and Rutherford, A.W. (1987). In the oxygen-evolving complex of photosystem II the S_0 state is oxidized to the S_1 state by D^+ (signal II_{slow}). Biochemistry *26*, 2401–2405.

Styring, S., Sjöholm, J., and Mamedov, F. (2012). Two tyrosines that changed the world: interfacing the oxidizing power of photochemistry to water splitting in photosystem II. Biochim. Biophys. Acta *1817*, 76–87.

Suga, M., Akita, F., Hirata, K., Ueno, G., Murakami, H., Nakajima, Y., Shimizu, T., Yamashita, K., Yamamoto, M., Ago, H., and Shen, J.-R. (2015). Native structure of photosystem II at 1.95 Å resolution viewed by femtosecond X-ray pulses. Nature *517*, 99–103.

Szczepaniak, M., Sugiura, M., and Holzwarth, A.R. (2008). The role of Tyr_D in the electron transfer kinetics in photosystem II. Biochim. Biophys. Acta *1777*, 1510–1517.

Tommos, C., Hoganson, C.W., Di Valentin, M., Lydakis-Simantiris, N., Dorlet, P., Westphal, K., Chu, H.-A., McCracken, J., and Babcock, G.T. (1998). Manganese and tyrosyl radical function in photosynthetic oxygen evolution. Curr. Opin. Chem. Biol. *2*, 244–252.

Umena, Y., Kawakami, K., Shen, J.-R., and Kamiya, N. (2011). Crystal structure of oxygen-evolving photosystem II at a resolution of 1.9 Å. Nature *473*, 55–60.

Un, S., Brunel, L.-C., Brill, T.M., Zimmermann, J.-L., and Rutherford, A.W. (1994). Angular orientation of the stable tyrosyl radical within photosystem II by high-field 245-GHz electron paramagnetic resonance. Proc. Natl. Acad. Sci. U S A *91*, 5262–5266.

Un, S., Tang, X.-S., and Diner, B.A. (1996). 245 GHz high-field EPR study of tyrosine-D and tyrosine-Z in mutants of photosystem II. Biochemistry *35*, 679–684.

Young, I.D., Ibrahim, M., Chatterjee, R., Gul, S., Fuller, F.D., Koroidov, S., Brewster, A.S., Tran, R., Alonso-Mori, R., Kroll, T., et al. (2016). Structure of photosystem II and substrate binding at room temperature. Nature *540*, 453–457.

Zhang, C., Chen, C., Dong, H., Shen, J.-R., Dau, H., and Zhao, J. (2015). A synthetic Mn_4Ca-cluster mimicking the oxygen-evolving center of photosynthesis. Science *348*, 690–693.

Zhao, Y., Swierk, J.R., Megiatto, J.D., Sherman, B., Youngblood, W.J., Qin, D., Lentz, D.M., Moore, A.L., Moore, T.A., Gust, D., and Mallouk, T.E. (2012). Improving the efficiency of water splitting in dye-sensitized solar cells by using a biomimetic electron transfer mediator. Proc. Natl. Acad. Sci. U S A *109*, 15612–15616.

iScience, Volume *23*

Supplemental Information

HYSCORE and DFT Studies of Proton-Coupled Electron Transfer in a Bioinspired Artificial Photosynthetic Reaction Center

Dalvin D. Méndez-Hernández, Amgalanbaatar Baldansuren, Vidmantas Kalendra, Philip Charles, Brian Mark, William Marshall, Brian Molnar, Thomas A. Moore, K.V. Lakshmi, and Ana L. Moore

Supplemental Information

List of Supplementary Figures:

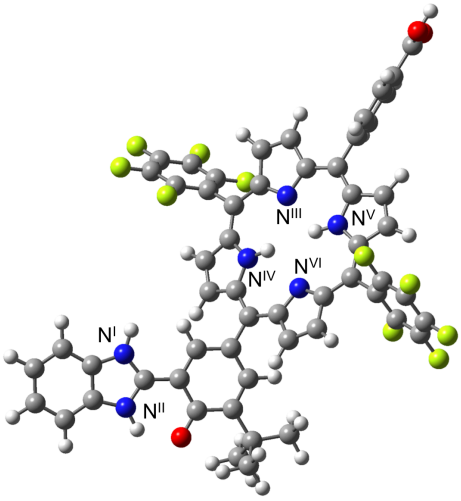

Figure S1: Related to Figure 5A. Schematic representing the numbering scheme of atoms in the **A** structure of the BiP–$PF_{10}^{\bullet+}$ PCET intermediate that was used in tabulating the results of the HYSCORE experiments and DFT calculations.

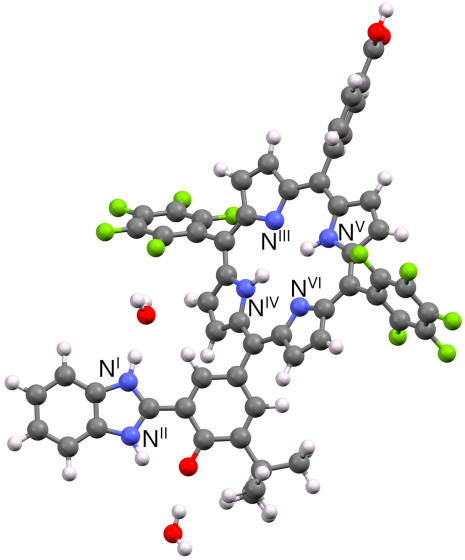

Figure S2: Related to Figure 5B. Schematic representing the numbering scheme of atoms in the **B** structure of the BiP–$PF_{10}^{\bullet+}$ PCET intermediate that was used in tabulating the results of the HYSCORE experiments and DFT calculations.

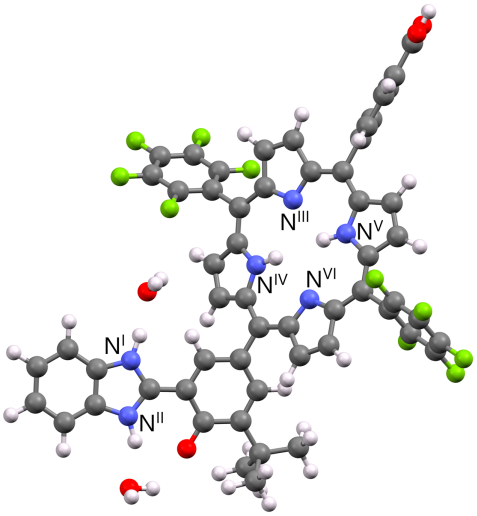

Figure S3: Related to Figure 5C. Schematic representing the numbering scheme of atoms in the **C** structure of the BiP–$PF_{10}^{\bullet+}$ PCET intermediate that was used in tabulating the results of the HYSCORE experiments and DFT calculations.

List of Supplementary Tables:

Table S1. Related to Table 1. The ^{14}N hyperfine and quadrupolar parameters that are obtained from DFT calculations of the **B** structure of the BiP–$PF_{10}^{\bullet+}$ PCET intermediate.

Nitrogen	**K (MHz)** (calculated **B** structure)	**A_{iso} (MHz)** (calculated **B** structure)
N^{I}	-0.67	0.86
N^{II}	-0.64	0.45
N^{III}	-0.81	3.00
N^{IV}	-0.73	0.65
N^{V}	-0.74	1.11
N^{VI}	-0.82	0.35

Table S2. Related to Table 1. The ^{14}N hyperfine and quadrupolar parameters that are obtained from DFT calculations of the **A** structure of the BiP–$PF_{10}^{\bullet+}$ PCET intermediate.

Nitrogen	**K (MHz)** (calculated **A** structure)	**A_{iso} (MHz)** (calculated **A** structure)
N^{I}	-0.61	1.01
N^{II}	-0.61	0.57
N^{III}	-0.80	2.45
N^{IV}	-0.75	0.59
N^{V}	-0.74	0.94
N^{VI}	-0.80	0.24

Table S3: The **g**-tensors that are obtained from the DFT calculations of the **A**, **B** and **C** structure of the BiP–$PF_{10}^{\bullet+}$ PCET intermediate.

Structure	g_X	g_Y	g_Z
A	2.0056	2.0042	2.0023
B	2.0052	2.0041	2.0023
C	2.0060	2.0044	2.0023

Transparent Methods

Synthesis and Characterization: BiP–PF_{10} was synthesized and characterized following the procedures reported by Megiatto *et al*. (Megiatto et al., 2012, 2014). The procedure consists of an acid-catalyzed porphyrin condensation of 5-formyl-3-tert-butyl-2-hydroxybenzaldehyde, 5-(pentafluorophenyl)dipyrromethane, and methyl-4-formylbenzoate at room temperature to form 5, 15-bis(pentafluorophenyl)-10-(4-methoxycarbonylphenyl)-20-(3-formyl-4-hydroxy-5-tert-butylpheynyl)porphyrin. After purification this porphyrin precursor was allowed to react with 1,2-phenylenediamine to form the ester form of the BiP–PF_{10}, 5, 15-bis(pentafluorophenyl)-10-(4-methoxycarbonylphenyl)-20-[2'-(3"-tert-butyl-2"-hydroxyphenyl)benzimidazole]porphyrin. Finally, the ester was hydrolyzed with trifluoroacetic acid and HCl to form the desired compound 5, 15-bis(pentafluorophenyl)-10-(4-carboxyphenyl)-20-[2'-(3"-tert-butyl-2"- hydroxyphenyl)benzimidazole]porphyrin.

Continuous-wave and Pulsed EPR Spectroscopy: The EPR spectra were obtained on a custom-built continuous-wave (*cw*)/pulsed X-band Bruker Elexsys 580 EPR spectrometer using a dielectric flex-line ER 4118-MD5 probe (Bruker BioSpin, Billerica, MA) and a dynamic continuous-flow cryostat CF935 (Oxford Instruments, Oxfordshire, U.K.) at 30 K temperature. The *cw* EPR spectrum of the BiP–$PF_{10}^{\bullet+}$ was acquired at the operating microwave frequency of 9.71 GHz with modulation frequency of 100 kHz, modulation amplitude of 1 G and microwave power of 0.7 μW. For the magnetic-field-sweep electron-spin-echo EPR spectrum, the primary electron spin echo was generated using the pulse sequence ($\pi/2$–τ–π–τ–echo). The echo was integrated over a 32 ns time window that was centered at the maximum of the echo signal. The length of the $\pi/2$- and π-pulse was 8 ns and 16 ns, respectively. The inter-pulse separation, τ, was 120 ns and the delay in the

pulse sequence is defined as the difference in the starting point of the pulses.

The 2D ^{14}N HYSCORE spectra were recorded at magnetic field position of 346.1 mT. For the 2D ^{14}N HYSCORE spectra of BiP, the echo amplitude was measured using the pulse sequence ($\pi/2$–τ–$\pi/2$–t_1–π–t_2–$\pi/2$–τ–echo) with a τ value of 136 ns, an 8 ns and 16 ns length for the $\pi/2$- and π-pulse, respectively. The delays in the pulse sequence are defined as the difference in the starting point of the pulses. The echo intensity was measured as a function of t_1 and t_2, where t_1 and t_2 were incremented in steps of 16 ns from an initial value of 40 ns and 32 ns, respectively. 256 steps were used for each dimension. The 8 ns time difference between the initial value of t_1 and t_2 was set to account for the difference in length between the $\pi/2$- and π-pulse. The unwanted echoes were eliminated by applying a 16-step phase cycling procedure. The hyperfine parameters of the ^{14}N nuclei were obtained by performing numerical simulations using the *saffron* function of the EasySpin software package (Stoll and Schweiger, 2006). The simulated spectra were carefully compared with the experimental ones to match the position of the cross-peaks and signal intensity distribution over the different points of the ridges.

The frequency of the double-quantum transition is described by the following equation:

$$\nu_{dq\pm} = 2[\nu^2_{eff\pm} + K^2(3 + \eta^2)]^{1/2}$$

The effective frequency is $\nu_{eff\pm} = |\nu_I \pm a/2|$ where ν_I is the nuclear Zeeman frequency for the given magnetic field and a is the hyperfine (isotropic) coupling value. The value of nuclear quadrupole coupling is described by $K = e^2qQ/4\hbar$ where Q is the quadrupole moment interacting with the electric field gradient q and η is the asymmetry parameter. In general, the isotropic hyperfine coupling is calculated from the cross-peak positions of the double-quantum transitions. The detection of cross-peaks in the (-,+) and (+,+) quadrant depends mainly on the strength of the electron-nuclear hyperfine coupling and orientation dependence of the nuclear transition of inequivalent ^{14}N nuclei.

Density Functional Theory Calculations: The theoretical structure of the **A**, **B** and **C** models of the PF_{10}–$BiP^{\bullet+}$ radical (**Figure 5A-C**) was optimized with Gaussian 09 (Frisch et al., 2009) at the B3LYP/6-31G(d,p) (Becke, 1996, 1988; Francl et al., 1982; Hariharan

and Pople, 1973; Lee et al., 1988; Rassolov et al., 1998) level of theory using the Conductor-like Polarizable Continuum Model (CPCM) (Barone and Cossi, 1998; Cossi et al., 2003) to simulate a dimethyl sulfoxide (DMSO) environment. The electron spin density distributions, quadrupolar and hyperfine coupling parameters and g-tensors for all of three structures were obtained with ORCA (Neese, 2018) at the B3LYP/EPR-II (Vincenzo et al., 2002) level of theory using the Conductor-like Screening Model (COSMO) (Klamt and Schüürmann, 1993), with the value of epsilon set to 47.2 and refrac at 1.479 to simulate a dimethyl sulfoxide (DMSO) environment.

Supplemental References

Barone, V., Cossi, M., 1998. Quantum Calculation of Molecular Energies and Energy Gradients in Solution by a Conductor Solvent Model. J. Phys. Chem. A 102, 1995–2001.

Becke, A.D., 1996. Density-functional Thermochemistry. IV. A New Dynamical Correlation Functional and Implications for Exact-exchange Mixing. J. Chem. Phys. 104, 1040–1046.

Becke, A.D., 1988. Density-functional Exchange-energy Approximation with Correct Asymptotic Behavior. Phys. Rev. A 38, 3098–3100.

Cossi, M., Rega, N., Scalmani, G., Barone, V., 2003. Energies, Structures, and Electronic Properties of Molecules in Solution with the C-PCM Solvation Model. J. Comp. Chem. 24, 669–681.

Francl, M.M., Pietro, W.J., Hehre, W.J., Binkley, J.S., Gordon, M.S., DeFrees, D.J., Pople, J.A., 1982. Self-consistent Molecular Orbital Methods. XXIII. A Polarization-type Basis Set for Second-row Elements. J. Chem. Phys. 77, 3654–3665.

Frisch, M.J., Trucks, G.W., Schlegel, H.B., Scuseria, G.E., Robb, M.A., Cheeseman, J.R., Scalmani, G., Barone, V., Mennucci, B., Petersson, G.A., 2009. Gaussian 09, Revision A. 1. Gaussian Inc. Wallingford CT 27, 34.

Hariharan, P.C., Pople, J.A., 1973. The Influence of Polarization Functions on Molecular Orbital Hydrogenation Energies. Theoret. Chim. Acta 28, 213–222.

Klamt, A., Schüürmann, G., 1993. COSMO: A New Approach to Dielectric Screening in Solvents With Explicit Expressions for the Screening Energy and Its Gradient. J. Chem. Soc., Perkin Trans. 2, 799–805.

Lee, C., Yang, W., Parr, R.G., 1988. Development of the Colle-Salvetti Correlation-energy Formula Into a Functional of the Electron Density. Phys. Rev. B 37, 785–789.

Megiatto, J.D.Jr., Méndez-Hernández, D.D., Tejeda-Ferrari, M.E., Teillout, A.-L., Llansola-Portolés, M.J., Kodis, G., Poluektov, O.G., Rajh, T., Mujica, V., Groy, T.L., Gust, D., Moore, T.A., Moore, A.L., 2014. A Bioinspired Redox Relay that Mimics Radical Interactions of the Tyr–His Pairs of Photosystem II. Nature Chem. 6, 423–428.

Megiatto, J.D., Patterson, D., Sherman, B.D., Moore, T.A., Gust, D., Moore, A.L., 2012. Intramolecular Hydrogen Bonding as a Synthetic Tool to Induce Chemical Selectivity in Acid Catalyzed Porphyrin Synthesis. Chem. Commun. 48, 4558–
Neese, F., 2018. Software Update: The ORCA Program System, Version 4.0. Wiley Interdisc. Rev.: Comp. Molec. Sci. 8, e1327.
Rassolov, V.A., Pople, J.A., Ratner, M.A., Windus, T.L., 1998. 6-31G* Basis Set for Atoms K Through Zn. J. Chem. Phys. 109, 1223–1229.
Stoll, S., Schweiger, A., 2006. EasySpin, A Comprehensive Software Package for Spectral Simulation and Analysis in EPR. Journal of Magnetic Resonance 178, 42–55.
Vincenzo, B., Alessandro, B., Carlo, F.P., 2002. Recent Advances in Density Functional Methods, Part III. World Scientific.